Journal of Manufacturing Processes 117 (2024) 213–223

Contents lists available at ScienceDirect

Journal of Manufacturing Processes

journal homepage: www.elsevier.com/locate/manpro

Study of the system instability impacts on surface characteristics for vibration-assisted AFM-based nanomachining

Xinchen Wang, Mohammad Alshoul, Huimin Zhou, Jia Deng, Zimo Wang *

Binghamton University, State University of New York, 4400 Vestal Parkway East, Binghamton, NY 13902, USA

ARTICLE INFO

Keywords:
AFM-based nanomachining
Nanodynamics
Surface characterizations
Gaussian process regression

ABSTRACT

Vibration-assisted atomic force microscopy (AFM)-based nanomachining is a promising method for the fabrication of nanostructures. During mechanical nanomachining, the geometry of the tooltip and workpiece interface is sensitive to variations in the depth of cut, the material grain size, and system vibrations; understanding the underlying uncertainties is essential to improve the process capability. This paper investigates process uncertainties and their impacts on the achieved surface geometries based on an experimental study of AFM-based nanomachining. The variations and biases of the achieved surface characteristics (compared to the theoretical geometries) are observed and identified as the torsional deflections on the AFM probe. A physical-based model combined with the Kriging method is reported to capture such uncertainties and estimate the surface finish based on different process parameters.

1. Introduction

The increasing demands of nanostructures in numerous applications, such as optical components, integrated electronics, and miniature sensors, necessitate the development of nanoscale manufacturing technology [1,2]. Compared to the energy beam-based nanomachining approaches [3], the cutting tool-based nanomachining is cost-effective with exquisite tunability [4,5]. Among mechanical nanomachining methods, atomic force microscopy (AFM)-based nanomachining is a promising method for fabricating complicated structures under the nanoscale due to its comparably high resolution [6–8] and capability of realizing complex structures [9–11] with high aspect ratios [12,13]. The AFM probe is applied as the machine tool for material removal, and the integrated mechanical vibrations enhance the material removal capabilities during nanomachining for different materials and fabrication conditions [14,15]. With the aid of in-plane circular motions, the material removal rate is significantly increased, and the cutting accuracy is improved by reducing the tool engagement time and instantaneous uncut chip thickness with less tip wear [16–19].

Currently, the critical issue of mechanical-based nanomachining resides in the surface integrity under the nanoscale [20]: During the vibration-assisted mechanical nanomachining, the tool tip type and radius of the AFM probe, the amplitudes of the mechanical vibrations, and the thickness of the material are within the same order of magnitude; the movements of the probe tooltip critically affect the geometric features of the cutting profiles [21–23]. Enabling nanofeatures with consistent cutting depths and desired cutting widths is important to improve the surface profile resolution. Particularly, the resolution in nanomachining refers to the finest surface profile geometry that can be obtained [24]; the highest resolution can be expressed as the minimal level of the cut width under the required depth and surface roughness. To increase the process accuracy, electromagnetic force has been used to control the tip displacement to ensure consistent cutting depth for the nanomachining process [25]. During the nanomachining processes, surface integrity issues such as defects and material pile-ups due to different tool path strategies under the nanometric level have been reported [26,27]. As one major factor in the achieved surface characteristics, the influence of different types of AFM probe tips (e.g., tip shape, rake angle, and different levels of wear) for nanochannels has been studied [28–30]. Understanding the relationship between the cutting features and the generated surface morphology is essential to ensure high resolution and precision for nanofabrication [31]. To investigate the mechanisms of generating surface profile under the nanoscale, a previous study [32] unveiled the material removal mechanisms (combined cutting with ploughing) under the nanometric level and reported a physical-based model to capture the tooltip-workpiece geometry during the process. The physical-based models for the relationships between surface morphology, tooltip dynamics, and geometric features have been reported [33–35]. To handle the machining uncertainty due to the negative rake angle of the probe tip, which may affect the precision and

* Corresponding author.

https://doi.org/10.1016/j.jmapro.2024.02.066
Received 27 October 2023; Received in revised form 8 February 2024; Accepted 28 February 2024
Available online 12 March 2024

accuracy of the achieved nanochannels, a power-law function has been presented to capture the tip bluntness during the tip-based nanofabrication [36,37]. Furthermore, molecular dynamics simulations were performed to investigate the combined effect of tip inclination and scratch direction on the nanofabrication morphology [38]. The displaced material and the associated pile-ups along the sides of the nanochannels generated during fabrication can modify the cutting profiles and consequently affect the precision of the surface finish; a pile-up removal strategy was proposed to preserve the shape and morphology of nanostructures [39,40]. He et al. [41] investigated the formation mechanism of such protuberances in the dynamic ploughing lithography (DPL) process. The dynamic response of the probe cantilever was considered in the scanning mode to characterize the protuberances along the nanochannels. Moreover, Yan et al. [42] studied the tip orientation effects on the achieved surface characteristics and pile-ups during the tip-based dynamic ploughing process. A comprehensive experimental case study was conducted in [43] to guide the design of the nanofabrication (selection of machining parameters) to minimize the surface integrity issues. Recent work was reported that connects the achieved surface characteristics to process parameters, such as the tip shape, feed, and downforces for AFM-based mechanical nanomachining [44,45]. Most existing studies on the relationship between tooltip dynamics and the resultant surface finish mainly focus on cutting depth as the primary metric [25], which may overlook three-dimensional (3D) morphology characteristics to evaluate the nanofabrication morphology. The relationships between different surface characteristics describing the 3D morphology have not been fully studied [46]. Moreover, very few studies reported the influence of dynamics instability on the achieved cutting profiles during AFM-based nanofabrication. However, the probe cantilever rigidity, cutting features with the relationships of other parameters may all affect the achieved cutting performance, and therefore, understanding the underlying dynamics and its relationship with the resultant surface morphology is critical to ensure machining precision and resolution of the established nanofabrication platform.

In this paper, we investigate the impact of nanodynamics on the resultant surface characteristics, specifically on the relationships between achieved profile depths and widths. The experimental case studies suggest that the system instability caused by piezoelectric actuators and the rigidity of the probe cantilever impacts the achieved surface profile characteristics. Such uncertainties can introduce an issue as to how to control the downforce to create acceptable nanolithography morphology with the desired minimal resolution (width of the trench). A physical model is then proposed to depict the geometric relationship between the tooltip and the workpiece interface to explore the uncertainties of the achieved nanochannels. To handle the process uncertainties, a Gaussian process regression (GPR) model combined with the presented physical model is applied to capture the relationships between the metrics of the surface morphology characteristics, namely, the cutting width and cutting depth. The prediction results indicate that the physical model can finely present the deterministic term associated with the cutting width, and the GPR model can effectively capture the uncertain item caused by vibration and downforce. The reminders of the paper are organized as follows: Section 2 introduces the experimental setup and initial sample observations; the developed physical model is described in Section 3; Section 4 presents the GPR model and validates the cutting width model by the GPR prediction results; Section 5 concludes the whole paper.

2. Experimental setup and data preprocessing

2.1. Hardware setup and the experiment description

The vibration-assisted AFM-based nanomachining experiments were conducted on a designed nanovibrator platform within a commercial AFM system (XE7, Park Systems Corporation, Suwon, South Korea), shown in Fig. 1 a). The nanovibrator consists of two piezoelectric actuators [PiezoDrive (SA050510, SA series), 150 V stack actuators] installed to vibrate the protruding aluminum pillar, providing high-frequency circular vibrations (2 kHz) in the *xy*-plane. A signal generator (USB-6259, National Instruments, Austin, TX, USA) and two signal amplifiers (PX200, PiezoDrive, Shortland, NSW, Australia) are used to generate the input signals for the piezoelectric actuators. These piezoelectric actuators are driven by sinusoid signals with a 90-degree phase difference and create in-plane vibrations for a polymethyl methacrylate (PMMA) sample (coated on a silicon substrate), which is fixed on the aluminum stage. The piezoelectric actuators with stable voltages can generate fixed vibrations (frequency and amplitude), which can greatly improve machining efficiency in the nanofabrication process compared to conventional static sample scratching. We conducted this experiment on a 200 nm thickness PMMA sample, spin-coated on silicon substrates with post-bake at 180 °C for 90 s. The diamond-like-carbon (DLC) AFM probe (DLC 190) [In Fig. 1 a)] was applied for the nanomachining of the PMMA sample. The probe cantilever's length, width, and thickness are 225 μm, 38 μm, and 7 μm, respectively. The force constant of the cantilever is 48 N/m. With assistance from the piezoelectric actuators in Fig. 1 a), the *xy*-direction vibrations can be generated on the sample/workpiece with the 90-degree phase difference driving signals, and these two directional vibrations combined with the line movement (0.5 $\mu m/s$) of the tip with fixed feed direction can create a circular movement on the surface as shown in Fig. 1 c) and d). The piezoelectric actuators allow a linear coefficient of 77 nm/V with an error of +/− 8 nm/V in displacement. During the cutting process, the cutting downforce is controlled by the AFM system, which dynamically maintains consistent cantilever deflections.

With the assistance of *xy*-plane vibration [1.6 VPP (Voltage of Peak-to-Peak) and 2 kHz], a set of nanochannels (with the length around 1 μm) were achieved by varying cutting forces (50, 150, 250, 350, and 450 nNs) on PMMA sample surface. The AFM microscopic image of the machined surface morphology is shown in Fig. 2 a). The feed direction of the tip is from the bottom to the top. The surface morphology characteristics, including the cutting depth and cutting width, are illustrated in Fig. 2 b); the cross-sectional line of the sample was extracted and plotted in Fig. 2 c). Fig. 2 d)-f) show the recording of the downforce signals during one cutting (trench 2)—the downforce signals are generated based on the laser point deflection from the AFM probe tip cantilever (calculated based on the deflection of the cantilever)—this downforce signal may be interfered with by the system vibrations, as suggested by the periodic patterns observed for both Fig. 2 d) and f). However, the downforce remains consistent during the non-cutting process in Fig. 2 d). Even when the material removal starts where the system vibrations increase, the downforce remains consistent during the nanomachining. The downforce signal can accurately quantify the cutting period with non-overshooting and undershooting before or after cutting, indicating the setpoint control's accuracy.

2.2. Feature extractions for surface characteristics

We further investigated the machined profiles on the PMMA sample: the 3D morphology of the five achieved trenches was generated by AFM microscopy, using a finer probe tip to ensure the precision of the scanned surface morphology. More metrics describing the achieved surface morphology and how to generate these measures are discussed in this subsection.

To observe the details of the cutting features, such as cutting depth, cutting width, and pile-ups, we remapped the trenches to the 3D coordinate in Fig. 3 with different views of the machined surface profile. Five trenches machined on a substrate of PMMA sample (within the area of 2 × $1.5\mu m^2$) using different cutting forces (50, 150, 250, 350, and 450 nNs) are shown in Fig. 3a) from left to right. The cutting depth, cutting width, and the direction of the cut are denoted and marked in Fig. 3 a) and b). The deep blue represents the valleys (surface profile under the

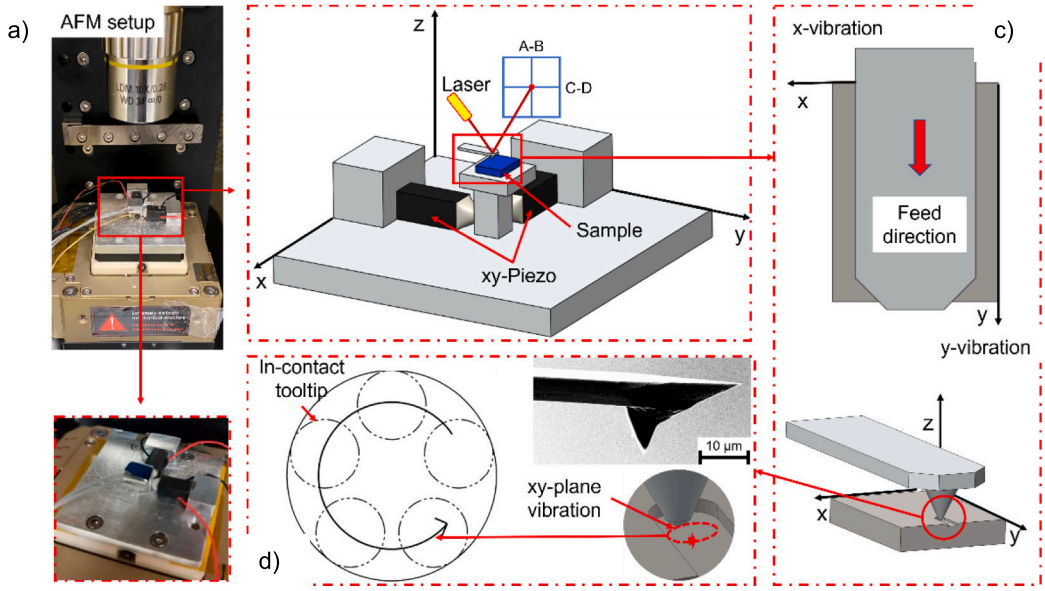

Fig. 1. a) Vibration-assisted AFM-based nanofabrication setup, b) the setup details, c) the cutting model of the probe and material, d) tool path of the nanomachining and tip morphology,

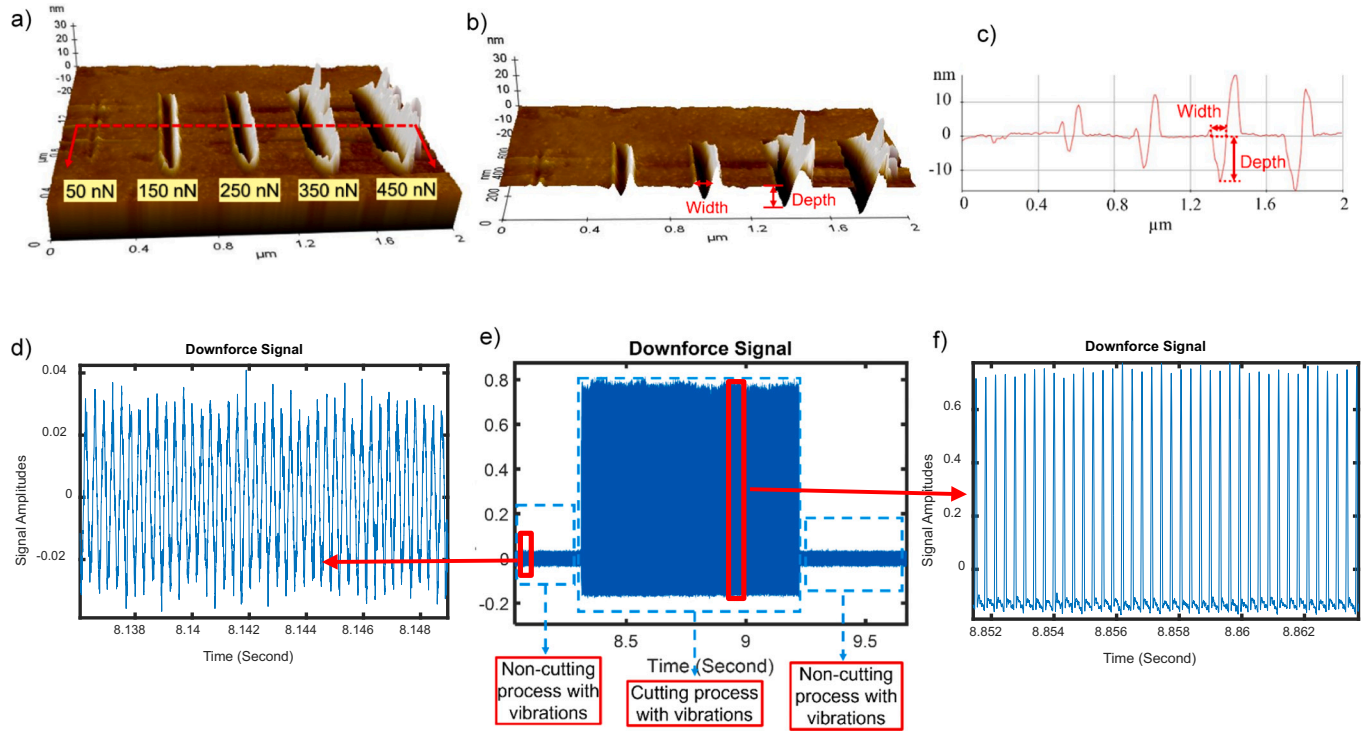

Fig. 2. a) Surface profiles of five trenches with five different cutting forces (50, 150, 250, 350, and 450 nNs) and cross-sectional line, b) cross-sectional morphology of the sample with cutting width and cutting depth notations, c) cross-sectional line of cutting profiles (depth and width), followed by the downforce signals recorded during the nanomachining; d) shows the downforce signal during the non-cutting process and cutting process, e) shows the details of downforce signal before the cutting process, and f) shows the details of downforce signal during the cutting process.

offset surface), and the red represents the peaks (pile-ups) on the sample surface. To ensure the surface morphology features are of high resolution, 256 by 192 data points, in total, are obtained based on the AFM scanned surface profile for the *xy*-plane of the machined PMMA sample separately. To ensure the precision of the sample data, the spline interpolation approach is used to enhance the resolution (a vector of 1200 points linearly spaced between and including the largest and smallest number of each axis), which can effectively avoid the Runge phenomenon and increase the precision of the acquired data [47].

The achieved depth and width of the machined nanotrench are used as two metrics to describe the trenches' morphology and evaluate the nanofabrication's precision. For the cutting depth, one can extract the depth line of each trench and project them to the *yz*-coordinates in Fig. 4 (Cut 3 is selected as an example to show the cutting depth line). In Fig. 4 c), (y, z) are the coordinates of one point on the cutting depth line. The absolute value of z is the depth value on this point, represented as D.

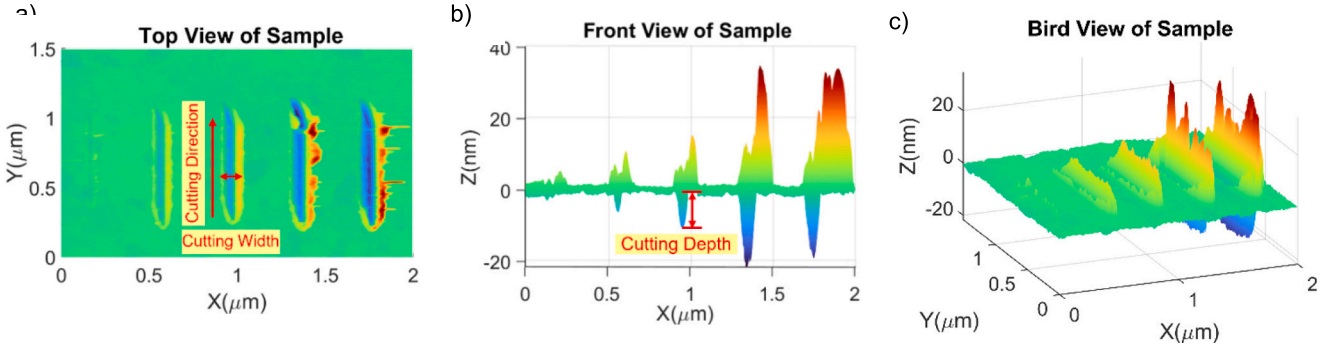

Fig. 3. a) Top view of cutting sample with cutting direction and cutting width notation, b) front view of cutting sample with cutting depth notation, c) bird view of cutting sample.

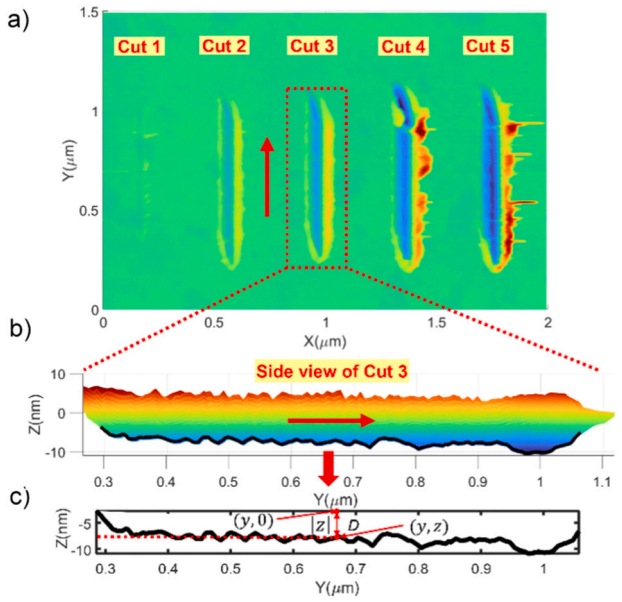

Fig. 4. a) Top view of the cutting sample with cutting direction (red arrow), b) and c) procedures of extracting the profile, specifically, the cutting depth: all cuts' depth can be projected to the *yz*-coordinate. The cutting depth value (absolute value of z) can be extracted from each data point on the cutting depth line and used as the surface features ($|z|$). (For interpretation of the references to colour in this figure legend, the reader is referred to the web version of this article.)

Due to the pile-up shown in Fig. 5 a), the cutting width boundary of the five trenches cannot be directly characterized [see Fig. 5 b)]. An offset to the surface height is applied, which creates a cross-sectional line on the trench to measure the cutting width [see Fig. 5 c)]. The width measured on the offset surface represents the whole trench's width. We set the offset as -1 nm in the z-axis (minimal value to allow partitions of the nanotrenches to surface pile-ups) to the surface plane so that minimal information is lost to the achieved surface characteristics. The achieved contours are red-boxed in Fig. 5 c). In addition, for some cuts with minimal downforce [see Cut 1 in Fig. 5 a)], we do not consider the sample(s) if there is no noticeable amount of material removed for further discussion.

The procedures of extracting the width of the cut for each trench are stated as follows: the cutting width boundaries are extracted from each trench on the *xy*-plane in Fig. 6 b), and the boundary line is projected to the *xy*-coordinate in Fig. 6 c) (Cut 3 is selected as an example). The width value of the cut (represented by L in Fig. 6 c)) can be obtained by subtracting the x coordinates of two points $[(y, x_{up}), (y, x_{down})]$ with the same y coordinate on the cutting width boundary line, and then taking the value of the subtracted result to represent the cutting width value $L = x_{up} - x_{down}$.

Based on the observations of the cutting depth and cutting width, the surface morphology at the end and the beginning of each cut exhibit different patterns, generally occurring during the cutting initiation and the tool drawing phase. Under the associated machining/cutting condition, the depth of cut (DoC) is in the same order of magnitude as the cutting tool tip radius (16 *nm* of the ball radius for the AFM-tip applied in the experiment) and the system vibrations. In addition, the unmachined surface can not be assumed to be flat (due to the scale we are considering at the nanoscale). This may be because at the initiation of the cutting tool (AFM probe tip), the dynamics come into play with burn-in time (tool-workpiece interface geometry initiates and changes). Similar to the cutting initiation, the tool drawing may introduce uncertainties as tool-workpiece interface geometry varies during the tool extractions.

In this paper, the modeling does not consider the surface characteristics during the cutting initiation and tool drawing phases. The cutting features obtained from these parts cannot reflect the stable cutting morphology, which should be discarded from further research.

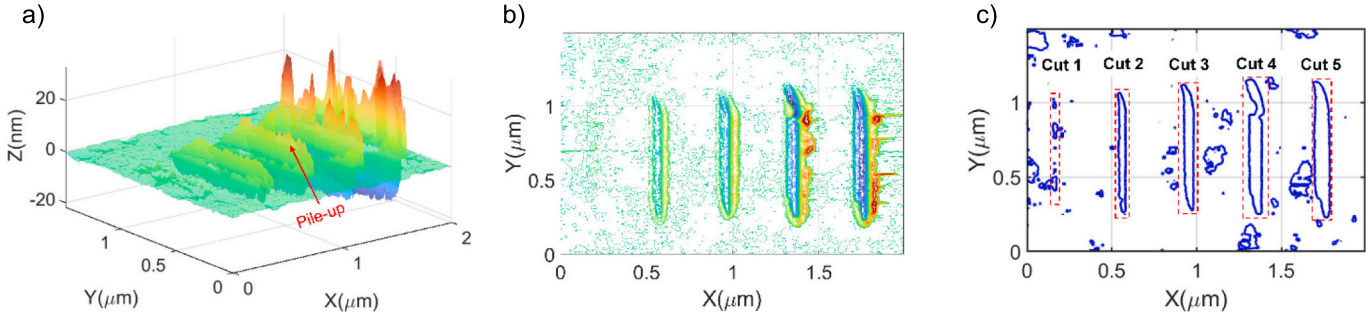

Fig. 5. a) Profile of the machined sample with the noticeable material pile-up, b) the top view of the transparent sample figure with contour line style, and c) the contour line of the sample at -1 nm z-axis position with cutting width boundaries of five trenches.

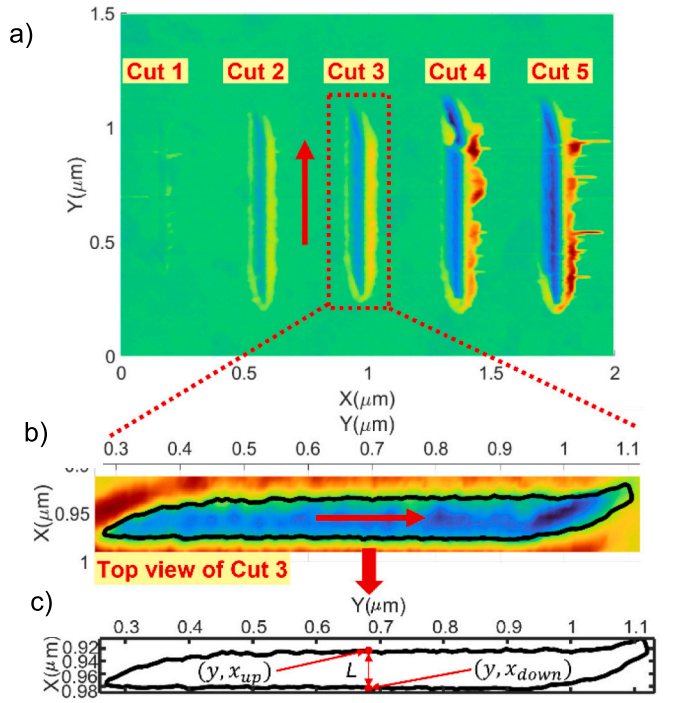

Fig. 6. a) Top view of the cutting sample with cutting direction (red arrow), b) and c) summarization of procedure for extracting the profile, specifically, the cutting width: all cuts' widths can be projected to the *xy*-coordinates. The cutting width value can be calculated by subtracting the *x* coordinate number of two points on the cutting width boundary with the same *y* coordinates and then taking the absolute value of subtracted results ($x_{up} - x_{down}$). (For interpretation of the references to colour in this figure legend, the reader is referred to the web version of this article.)

Therefore, only the portion with stable cutting for each trench is extracted for the analysis, and the corresponding cutting features are extracted synchronously from this cutting part in Fig. 7 (Cut 3 is selected as an example to show the segmentation process).

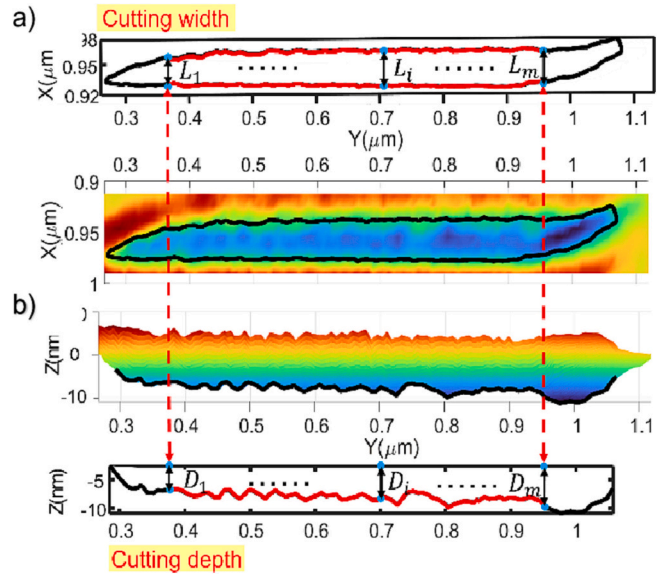

Fig. 7. a) Cutting width boundary line with width value notation (L_i), b) cutting depth line with depth value notation (D_i). The corresponding cutting depth and width values are collected from each trench without the initial and end parts.

In Fig. 7, the cutting depth lines and cutting width lines are extracted from the trench and plotted to the planes, and red lines on each coordinate mark the extracted portion of the surface profile features. The width and depth of the cut are the essential features to represent the nanochannel precision and quantify the material removal. To further explore the connection between the cutting depth and width, we synchronously collected extracted surface morphology characteristics (D, L) for each trench (Cut 2, Cut 3, Cut 4, and Cut 5), and the quantified cutting features (D_i,L_i) are marked in Fig. 7, where i is the index number of data points on segmented cutting profiles; m is the total number of data points on each trench; D_i is the empirical cutting depth value on ith data point, the depth value on the extracted trench can be represented as $D = \{D_1, D_2, \ldots, D_m\}$; L_i is empirical cutting width value on ith data point, the width value on extracted trench can be represented as $L = \{L_1, L_2, \ldots, L_m\}$.

As mentioned, the precision of the process refers to the minimal width achieved for the nanotrench while meeting the required cutting depth for the vibration-assisted AFM-based mechanical nanomachining. Investigating the relationship between geometric metrics may help understand the fundamental mechanisms under circular rotation/vibration-assisted mechanical nanomachining processes. These observations may support further analysis of the achieved surface characteristics.

3. Impacts of the process nanodynamics on resultant surface characteristics

3.1. Observation of the surface morphology characteristics

The generated surface characteristics for different cuts (Cut 2, Cut 3, Cut 4, and Cut 5), namely, the extracted surface features in pairs of (D_i, L_i), are plotted in Fig. 8, where the *x*-axis is the cutting depth, and the *y*-axis is the cutting width. Four groups are plotted using distinct colors, suggesting each cut group (see legend in Fig. 8). Essentially, this scatter plot represents the relationship between depth and width. Noticeably, by comparing the observations across groups (different cuts), the linear relationship between the trenches' depth-width is observed. In addition, the means of cutting depths and widths increase as the cutting downforce increases, though noticeable variations are observed for achieved trenches' widths and depths within each cutting. Based on the trench morphology observed in Fig. 8, the cutting width achieved by the vibration-assisted AFM nanofabrication increases with the deeper depths of the trenches, which is unlike mechanical-based

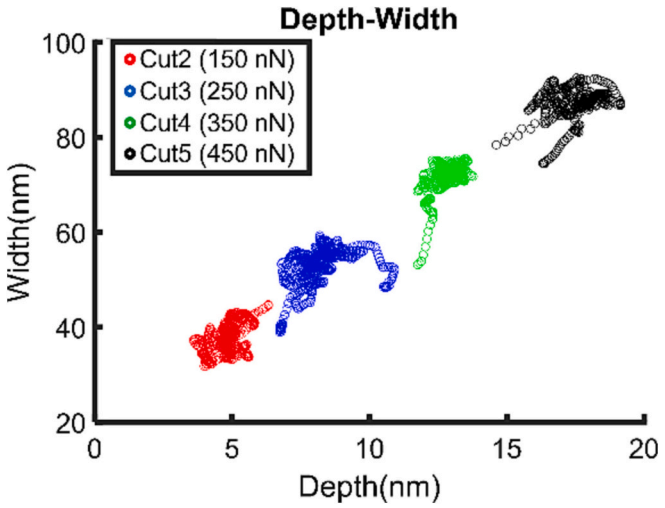

Fig. 8. Depth-width scatter plots of Cut 2, Cut 3, Cut 4, and Cut 5. The data sets of four trenches in coordinate show an obvious linear relationship between the cutting depth and cutting width.

machining under micro- and macro-machining, such as the end milling process, where the downforce/cutting force does not affect the width of the generated surface morphology [48]. As aforementioned, the cut's minimal width suggests the setup's capability to realize the finest geometry of the surface profile (i.e., the resolution of the setup). This find-out raises the question about the relationship between the downforce and the achieved surface characteristics and how to control parameters for achieving the desired cut depth while meeting the resolution requirement (width of the nanotrench). To understand the factors causing the above findings, we further develop an explicit model to depict the vibration-assisted nanomachining process and investigate the main reasons causing such different patterns in the relationships between surface geometric features with increasing cutting forces.

3.2. Modeling of the achieved surface morphology

The cutting profiles of the vibration-assisted AFM-based nanomachining significantly differ from the traditional nanochannels processed by tip-based scratches, especially the diverse cutting width value among the different cutting force conditions. Therefore, we propose a model for the vibration-assisted AFM-based nanomachining process to depict and quantify the cutting width. The model discussed in this paper is under the nanoscale, and the matrix of the trench is in the same order of magnitude compared to the cutting tool tip radius and the system vibrations. Therefore, the conventional deterministic model (mechanics) may not be adequate under such a scale because the uncertainties existing in the system may play a fundamental role in determining the surface characteristics.

Geometrical relationships among different parts in nanofabrication can determine the cutting width features. To figure out this relationship, we first investigate the machining process without the vibration assistances (static condition/simple scratches) in Fig. 9 a). To ensure the effectiveness of the model, the cutting-depth data are all collected from the stable part of each trench in Fig. 7. The machining tool tip radius (~15 nm) is comparable to the chip thickness; therefore, the cutting tool forms a negative rake angle. One can establish an explicit model to describe the geometric relationships among the tooltip, uncut chip thickness, and the achieved surface morphology based on the illustrated schematic diagram shown in Fig. 9 b). In Fig. 9 b), r represents the radius of the probe, c is the absolute value of the offset along the z-axis, and D is the cutting depth obtained from the depth line; w is the theoretical width of the in-contact cutting tooltip across the cross-section of the workpiece in this static nanofabrication process model. Then, w can be formulated as:

$$w = 2 \times \sqrt{r^2 - (r - (D - c))^2} \tag{1}$$

In this model, the AFM tip shape is represented by the cone with a spherical top (dashed circle line); the dashed line on the PMMA workpiece is the machined area. Based on the shape and position of the tooltip in Fig. 9 b), the w can also be regarded as the theoretical diameter of the cross-section of the in-contact probe tip projected onto the xy-plane in the static nanofabrication model.

Next, we extend this model to capture the tool trajectory by adding the rotary displacement from the mechanical vibration. The rotary movement generated by the system vibration couples with the feed of the probe (linear movement along the cutting direction) and consequently complicates the analysis of the nanomachining process. Fig. 10 a) depicts the top view of the trajectory of the tool motions. The red circles are the cross-section of the in-contact probe tip projected onto the xy-plane. The magenta-dotted circles represent the theoretical probe trajectory in rotary motions coupled with the feed, which moves along the feed direction.

In Fig. 10 a), the w is the theoretical diameter of the cross-section of the in-contact probe tip projected onto the xy-plane, which is the same one in Fig. 9, $\mathscr{L}$ is the theoretical cutting width of the trench with vibration assistance, and R is the theoretical diameter of the magenta-dotted circle, suggesting the amplitude of the system vibrations. To explore the geometric relationship among each object under the rotary vibrations, a side view of the nanomachining process is illustrated in Fig. 10 b), where the dotted lines depict the morphology of the AFM probe driven by the piezoelectric actuators. Here, the shape of the probe's tip and PMMA sample are simplified by the geometrical schematic. Fig. 10 c) shows the geometric relationships of each object based on the side view provided in Fig. 10 b). The corresponding parameters are marked in Fig. 10 c). Based on the analysis of the model, the theoretical trench width ($\mathscr{L}$) under vibration can be represented by:

$$\mathscr{L} = w + R \tag{2}$$

Considering the different cutting depth values on each trench, the theoretical cutting width $\mathscr{L}$ should also display a variation among different cuts based on the model (Eq. (2)). To verify the effectiveness of the model and find the reason for the cutting width fluctuation, the theoretical value ($\mathscr{L}$'s) acquired from the model should be compared with the empirical width (L) extracted from the trenches' figures to unveil the generation of cutting width during the nanofabrication process.

To investigate the variation of the cutting width, Fig. 11 shows the procedure to extract the empirical cutting width data (L) and represent them in a time series manner: Fig. 11 a) is the top view of the trench (Cut 3 is selected as an example). The data collected from Fig. 11 a) is then projected onto Fig. 11 b), where the y-axis represents the absolute values for the cutting width and the x-axis maintains the same resolution along the cutting direction.

It may be noticed that the actual cutting widths (L) not only exhibit significant variations among different trenches (in Fig. 8) but also fluctuate in the single trench (in Fig. 11), which contradicts the consistent tool tip trajectory as the vibration amplitude for the nanovibrator is set as a constant for the cutting under all conditions. To investigate the uncertain factors in cutting width, the items in the

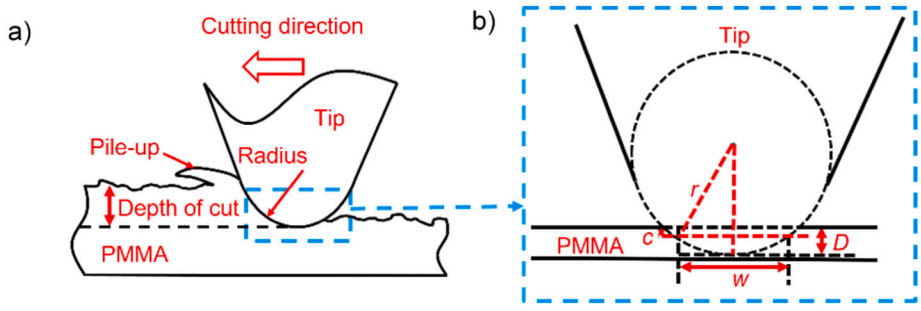

Fig. 9. a) Schematic diagram of the tooltip-workpiece interface between the AFM probe tip and the PMMA sample without vibration assistance, b) geometric relationships between the probe tip and the sample with annotated tip radius r, the cutting depth D, the absolute value of the offset c, and cutting width w without vibrations.

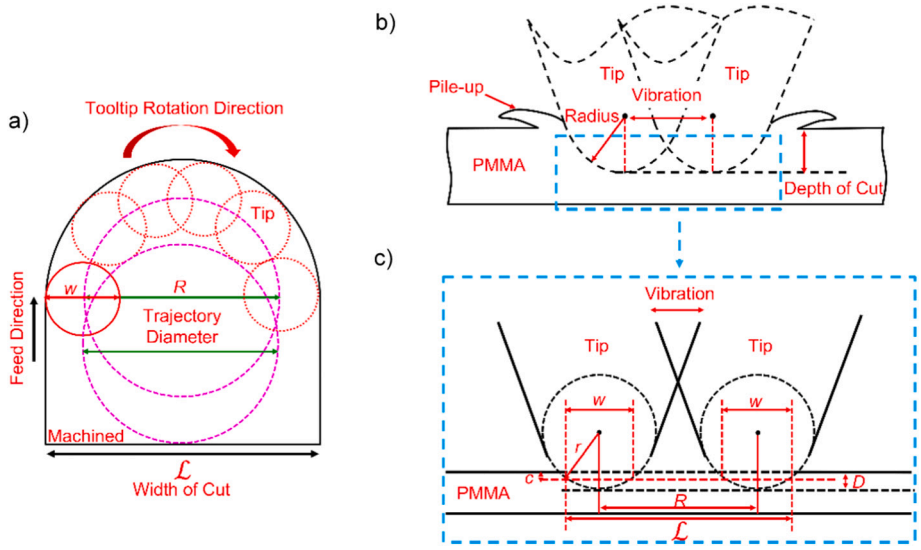

Fig. 10. a) Top view of nanomachining process schematic with AFM probe trajectory notation under vibration, b) side view of nanomachining process schematic with vibration, c) geometrical schematic of cutting model for AFM probe and PMMA sample with vibration.

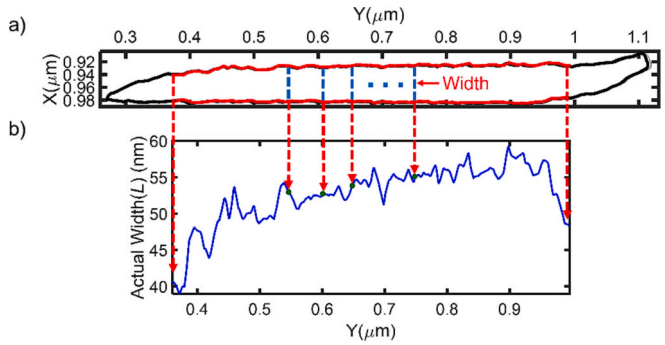

Fig. 11. a) The data of the cutting width values are extracted from the trench boundary contour and then mapped one-to-one into time series in b), where each point represents the absolute value of the cutting width right on the exact spot on the nanotrench.

theoretical cutting width model should be calculated on each trench using actual cutting depths (D) and compared with the empirical cutting width (L) to explore the unstable reason.

Firstly, the model-based theoretical cross-section diameter (w's) (Eq. (1)) is plotted to compare with the empirical cutting depth (L), as shown in Fig. 12.

In Fig. 12, the blue lines represent the empirical cutting width (L), and the red dotted lines represent the theoretical cross-section diameter for the in-contact probe tip (w's). One may notice that the variation of model-based results (w's) has similar patterns to the uncertainties in cutting width (L). This observation indicates that the proposed model can effectively capture the variation of the cutting width, and theoretical w can be regarded as one part of the cutting width. Furthermore, the similar patterns between L and w's in each trench indicate that the tip trajectory diameter (R's) value is stable in every single cut (by Eq. (2)) but fluctuates among trenches under different force conditions.

To show the trend of the variations in tip trajectory diameter across diverse cutting conditions, the tip trajectory diameter (R) is calculated by subtracting w from the empirical cutting width (L) (by Eq. (2)), and the mean values for the cutting depth (D) and tip trajectory diameter (R's) of each trench are plotted in Fig. 13.

It may be noticed that the cutting depth and probe trajectory diameter exhibit a linear relationship: as shown in Fig. 13, the means of $\{R\}$ increase as the downforce increases. Therefore, the relationship between the cutting depth (D) and tip trajectory diameter (R) can be expressed as:

$$R(D) = aD + b \tag{3}$$

where cutting depth (D) can be regarded as the independent variable for the tip trajectory diameter (R), a is the slope parameter, and b is the constant (intercept) parameter in the above equation. Moreover, the tip trajectory diameter (R) takes a comparatively large proportion of the achieved cutting width against the cross-section diameter w. However, the tip trajectory diameter (R) should be stationary as the vibration amplitude is set as a constant by the nanovibrator system. The changing R value during the nanofabrication under different force conditions can influence the resolution of the achieved nanochannel and increase the difficulty of the process control. Figuring out the reason for the unstable tip trajectory is essential to achieve monitoring for the nanofabrication under the dynamic system.

In the vibration-assisted AFM-based nanomachining process, the vibration amplitude essentially determines the geometry of the probe trajectory via the created circular motions in the xy-plane. However, significant variations are observed in different trenches. The results based on previous investigation suggest that the uncertainty component can be caused by cantilever torsional deflections of the probe (in Fig. 14) under different downforces. Fig. 14 lists the deflection of the probe for scratching and the condition of the torsional deflection with the system vibrations. In Fig. 14 a), the cantilever deflection can cause the tip to swing left and right with an angle during the nanofabrication. Compared to the existing studies where the AFM probe cantilever is under vibrations along the vertical direction [52,53], the presented setup—with system vibration introduced in both the lateral direction and longitudinal directions—may have complicated deflections due to the circular motions in xy-plane introduced by the system vibrations coupled with the cutting downforce. Such deflections can influence the precision of the probe tip movement during the nanofabrication process and consequently cause inconsistent tooltip trajectories under different downforces undertaken. Understanding the relationship between the levels of the defections due to the downforces and the resultant tool tip trajectory (R) is critical to allow estimations of the achieved surface characteristics. The downforce and the vibration can generate vertical and horizontal wobbling on the cantilever of the probe, which can impact the performance of the nanomachining process [51–53].

To investigate the influence of the torsional deflections on the achieved surface morphology, three levels of different torsional deflections

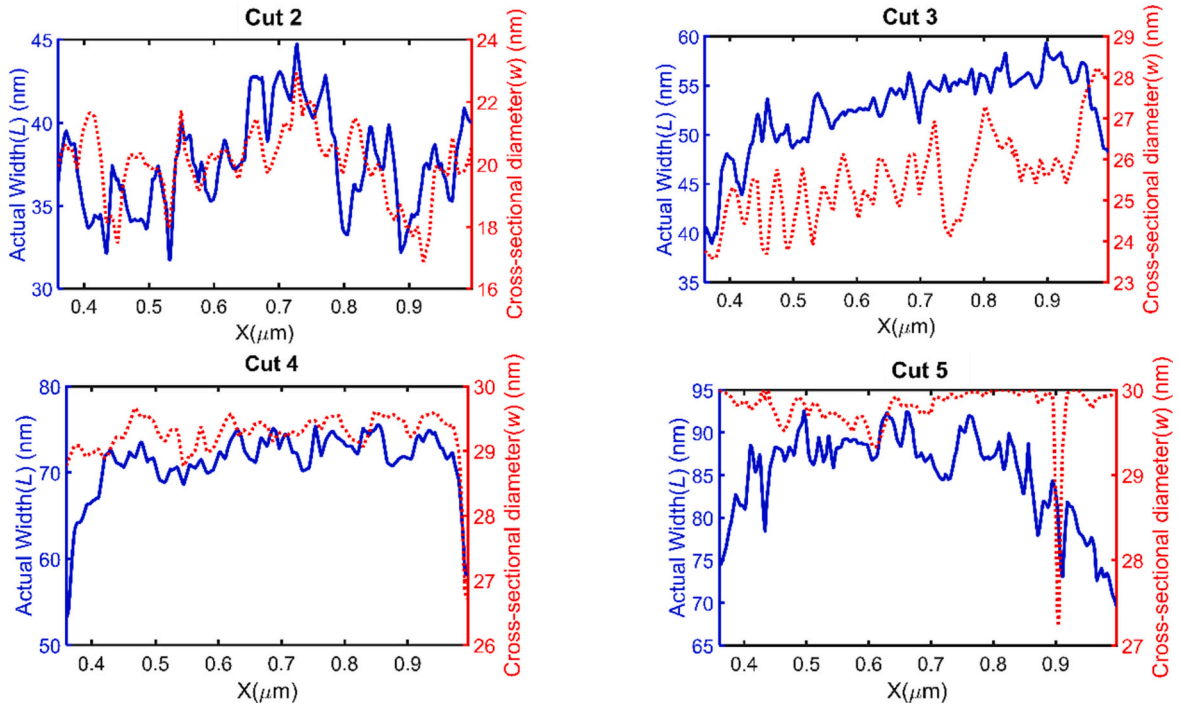

Fig. 12. Variation line of actual cutting width (L) and cross-section diameter for the in-contact probe tip (w's).

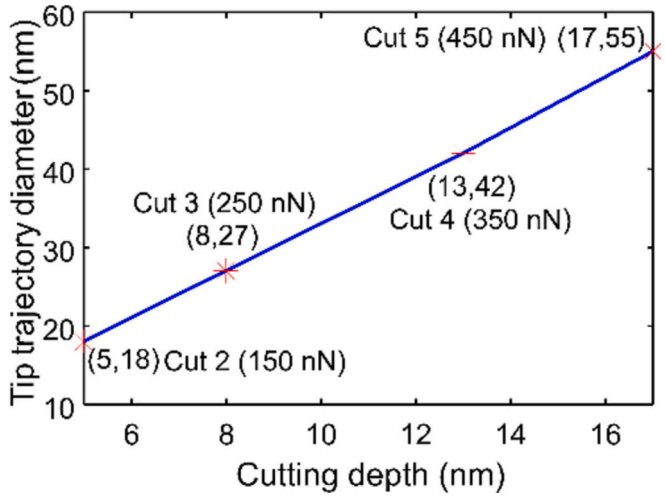

Fig. 13. a) Relationship between the mean value of cutting depth (D) and the mean value of probe trajectory diameter (R).

are depicted in Fig. 14 b). In Fig. 14 b), the first column illustrates the probe without the deflections ($\theta = 90^{\circ}$), and the corresponding geometric figures are plotted to show the relationship between the cutting width and probe shape. Meanwhile, two deflection conditions, inward ($\theta > 90^{\circ}$) and outward ($\theta < 90^{\circ}$) direction deflection, are plotted on the next two columns with their geometric figures. Comparing different conditions in Fig. 14 b), the probe with a cutting angle (θ) caused by torsional deflection can enlarge the cutting width with the same probe's tip shape and size. Therefore, the torsional deflection of the probe can be considered a significant factor that causes the changes in cutting width.

Based on our experiments, the torsional deflections of the AFM probe can be the reason for the different performances of the AFM probe under different loading conditions. The larger the downforce applied, the bigger the probe cantilever's amplitude. The torsional deflections are difficult to model explicitly due to the variations, such as system vibrations and probe spring constants, so a machine learning-based approach incorporated with the explicit tooltip geometry model is presented to capture the process variance due to the instability of tooltip dynamics and accurately predict the achieved surface geometry relationships.

4. Machine learning approach for predicting surface profiles with vibration uncertainty

4.1. Gaussian process regression model

The cutting width in the explicit model is combined with the probe trajectory diameter (R) and the in-contact tooltip diameter (w). Based on the above discussion, the instantaneous w can be calculated by the corresponding cutting depth, probe radius, and contour line position, which can be regarded as a deterministic term of the width. However, the probe trajectory diameter (R) influenced by the deflections of the AFM tip cantilever cannot be calculated directly: the spring constant for each probe may vary, and calibrations may be time-consuming. In addition, other process parameters may also introduce the variations, including microstructure/localized variations on the material strength and tooltip radius variations. All of these may introduce uncertainties in nanomachining. Therefore, we present a machine learning-based approach incorporating the explicit model to handle the deterministic term in the machining while the applied statistical model captures the process uncertainties.

The Gaussian process regression (GPR) is an effective machine learning method to handle nonlinear variation patterns by capturing the correlation between variables [54]. To depict the cutting width during the nanofabrication, we use the GPR model to predict the various width values on each position of the achieved trenches, where the cutting depth (D) is regarded as the input, and the cutting width ($\mathscr{L}$) is the output. The Gaussian Process (GP) in our case can expressed as [55,56]:

$$\mathscr{L}(D) \sim GP(m(D), k(D, D^{'})) \tag{4}$$

where $\mathscr{L}(D)$ is the cutting width function with the input cutting depth (D), $m(D)$ is the mean function, and $k(D, D^{'})$ is the covariance function.

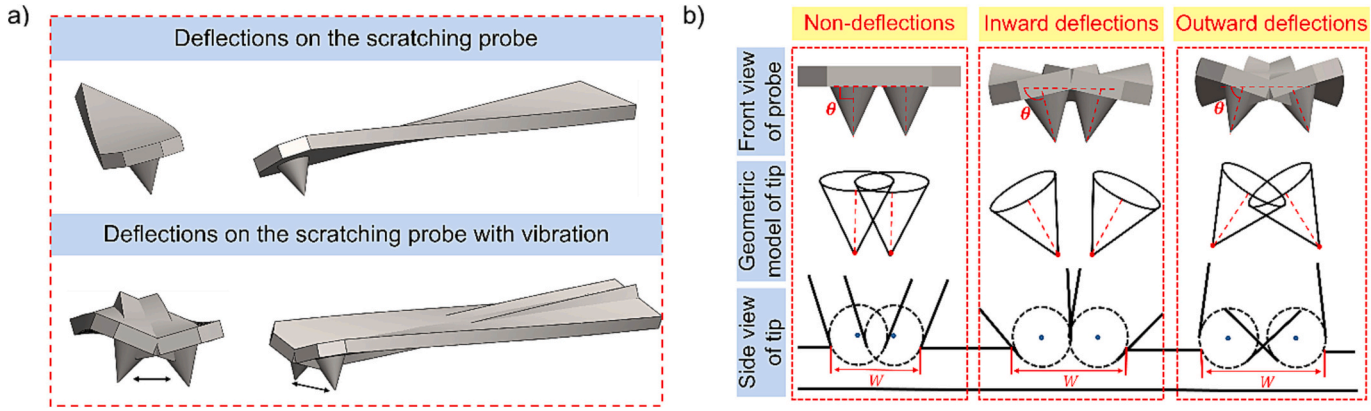

Fig. 14. a) The front view and side view of the AFM probe with torsional deflections during the scratching movement. Figures in the first row show the torsional deflection on the signal probe without vibration, and figures in the second row show the torsional deflections of the probe with vibration. The movement of the cantilever and tip under vibration conditions can be observed in the second column figures; b) schematic diagram of the non-deflection and deflection conditions with different cutting angles (θ). Two deflection conditions can result in a larger cutting width value than the non-deflection condition.

The covariance function in GP models the dependence between the function values at different input points, which can be expressed as:

$$k(D,D^{'}) = \mathbb{E}\left[(\mathscr{L}(D)-m(D))(\mathscr{L}(D^{'})-m(D^{'}))\right] \tag{5}$$

In our model, we select an independent covariance function, which is specified as:

$$k(D_p,D_q) = \sigma_n^2\delta_{pq} \tag{6}$$

where σ_n^2 is the noise variance and δ_{pq} is the Kronecker function, which equals 1 when $p=q$ and 0 otherwise [57].

The mean function in the GP model reflects the expected function value at input D (cutting depth). In our model, the mean function can be written as:

$$m(D) = \mathbb{E}[\mathscr{L}(D)] \tag{7}$$

To increase the prediction accuracy, we rewrite the prior mean function based on our theoretical cutting width model (in Eq. (2)), which can be written as:

$$\mathscr{L}(D) = w(D)+R(D) \tag{8}$$

where D is the cutting depth, $\mathscr{L}(D)$ is the cutting width function, $w(D)$ is the function of the cross-section diameter of the tooltip, and $R(D)$ is the function of the probe trajectory diameter.

The $w(D)$ in Eq. (2) ($w = 2\times\sqrt{r^2-(r-(D-c))^2}$) can be simplified as:

$$w = 2\times\left((2r+2c)D-D^2-2rc-c^2\right)^{\frac{1}{2}} \tag{9}$$

where the cutting depth D is the only independent variable in the equation, and the other item can be treated as the parameters in the Gaussian process model. The parameters formate of the $w(D)$ can be written as:

$$w(D) = \left(c_1D+c_2D^2+c_3\right)^{\frac{1}{2}} \tag{10}$$

where the parameters are replaced by coefficients c's.

The $R(D)$ in Eq. (3) ($R(D) = aD+b$) also can be represented as the parameter format, which is written as:

$$R(D) = c_4D+c_5 \tag{11}$$

Therefore, the mean function can be written as:

$$m(D) = \mathbb{E}\left[\left(c_1D+c_2D^2+c_3\right)^{\frac{1}{2}}+c_4D+c_5\right)\right] \tag{12}$$

where c_1, c_2, c_3, c_4, and c_5 are the parameters, and the cutting depth (D) is the input in the model. With the redefined mean function, the independent covariance function is selected as the kernel function in GPR to predict the cutting width. The predicted cutting width value (estimation in GPR) can be represented as $\widetilde{\mathscr{L}}(D)$:

$$\widetilde{\mathscr{L}}(D) = \sum_{i=1}^{t} b_i k(D_i,D) \tag{13}$$

where b_i represents the weight, and i represents the index of new inputs of cutting depth values ($i=1,2,\ldots,t$) [58].

The improved GPR model is applied to predict the cutting width on each trench and the predicted results ($\widetilde{\mathscr{L}}(D)^{'}s$) are compared with the empirical cutting width (L) to evaluate the effectiveness of the proposed physical model and the performance of the GPR model.

4.2. Prediction results of cutting width

Based on predicted results, the GPR model combined with the physical model effectively captures the uncertainty (probe's cantilever deflection) in cutting width caused by the vibration during the nanofabrication. The predicted cutting width line can mostly depict the variation of width value. Fig. 15 shows the actual and predicted width results of all cuts, where the red line is the predicted width data of the trench ($\widetilde{\mathscr{L}}(D)^{'}s$), and the blue line is the empirical cutting width value (L). Meanwhile, the 95 % prediction intervals are marked by grey shades on the prediction result figures.

The R-squared value and the RMSE value are listed in Table 1. The average values of R-squared and RMSE are 0.8962 and 0.8510, respectively, which indicate that the proposed model can effectively assist the GPR model in capturing the variation of the width changes during nanofabrication. The RMSE achieves a mean of 0.8510 among all trenches, which verifies that the GPR method combined with the physical cutting width model is stable for inferencing the cutting widths based on the cutting depths. This approach offers a new perspective to understanding the nanofabrication mechanism and proposes a potential method to monitor the machining process under the nanoscale.

5. Conclusion

In this paper, we observe the uncertain performance of the AFM probe during the vibration-assisted AFM-based nanomachining process, which significantly influences the cutting width under the nanoscale. A physical model for the cutting width is established to explore the

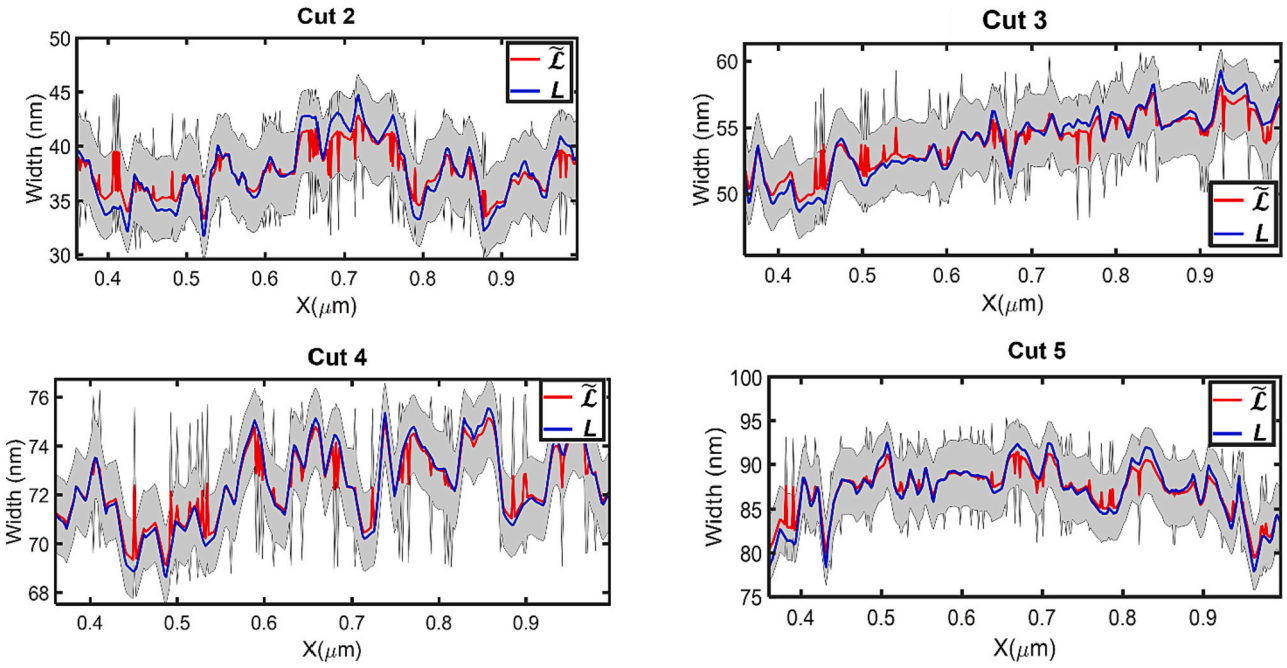

Fig. 15. The original width variation, predicted width variation, and 95 % prediction intervals of the trenches.

Table 1
Statistic description for *R*-squared value and RMSE for the predicted models.

	Cut 2	Cut 3	Cut 4	Cut 5	Average value
R-squared	0.8579	0.9005	0.9134	0.9128	0.8962
RMSE	1.2273	0.7660	0.4895	0.9207	0.8510

potential factors that cause the variation of nanoscale width and assist machine learning in predicting cutting morphology. The main contributions can be summarized as follows:

1) We studied the relationships between different surface morphology characteristics, specifically, each trench's complete width and depth value rather than the mean value. After visualizing and analyzing the experimental results, it suggests that the cutting width and cutting depth of trenches increase with the cutting downforce, and the linearity between the cutting width and depth can be observed under process uncertainties. Compared to conventional machining, the mechanical nanomachining process exhibits more significant variations under the nanoscale due to the same order of magnitude for tooltip radius, material grain size, system vibration, and the observed instability caused by probe/cantilever deflections.
2) The physical model for cutting width considering the in-contact part of the probe and tip trajectory (vibration amplitude) is established to explore the uncertainty factor for the nanofabrication. The torsional deflections on the probe are regarded as an important factor for the variation of the tip trajectory diameter, which can change the cutting width with the required cutting depth and downforce. The larger downforce will machine a deeper depth on the sample and enlarge the cutting width. That is, the system rigidity needs to be considered in influencing the process precision/resolution under nanofabrication.
3) A Kriging-based prediction method that incorporates the physical model while providing capability toward handling the process uncertainties for AFM-based mechanical nanomachining is presented. The prediction results suggest that the machine learning model with combined deterministic physical modeling on the tool tip geometry can accurately capture the relationship between different surface characteristics with complicated torsional deflections during nanomachining. In future work, the probe tip geometry due to the wear will be considered a significant factor in our contact physical model, influencing the cutting results under the nanoscale. In addition, the surface inconsistency at the cutting initiations and the tool extractions will be studied to add knowledge on understanding the mechanisms/dynamics when the tool-workpiece geometry varies.

Declaration of competing interest

The authors declare that they have no known competing financial interests or personal relationships that could have appeared to influence the work reported in this paper.

Acknowledgments

This work was supported by the National Science Foundation No. CMMI-2006127; the Binghamton University Data Science Transdisciplinary Areas of Excellence (TAE) seed grant; and the Small Scale Systems Integration and Packaging (S3IP) Center of Excellence from the New York Empire State Development's Division of Science, Technology, and Innovation.

References

[1] Mathew PT, Rodriguez BJ, Fang F. Atomic and close-to-atomic scale manufacturing: a review on atomic layer removal methods using atomic force microscopy. Nanomanufacturing Metrol 2020;3:167–86. https://doi.org/10.1007/s41871-020-00067-2.
[2] Gozen BA, Ozdoganlar OB. Design and evaluation of a mechanical nanomanufacturing system for nanomilling. Precis Eng 2012;36:19–30. https://doi.org/10.1016/j.precisioneng.2011.06.001.
[3] Zhou H, Jiang Y, Dmuchowski CM, Ke C, Deng J. Electric-field-assisted contact mode atomic force microscope-based nanolithography with low stiffness conductive probes. J Micro Nano-Manuf 2022:10. https://doi.org/10.1115/1.4054316.
[4] Tseng AA. Advancements and challenges in development of atomic force microscopy for nanofabrication. Nano Today 2011;6:493–509. https://doi.org/10.1016/j.nantod.2011.08.003.
[5] Chang S, Geng Y, Yan Y. Tip-based nanomachining on thin films: a mini review. Nanomanufacturing Metrol 2021. https://doi.org/10.1007/s41871-021-00115-5.
[6] Zhou H, Dmuchowski C, Ke C, Deng J. External-energy-assisted nanomachining with low-stiffness atomic force microscopy probes. Manuf Lett 2020;23:1–4. https://doi.org/10.1016/j.mfglet.2019.11.001.

[7] Stauffenberg J, Ortlepp I, Reuter C, Holz M, Dontsov D, Schäffel C, et al. Investigations on long-range AFM scans using a nanofabrication machine (NFM-100). In: 4th Int. Conf. NanoFIS 2020 - Funct. Integr. Nanosyst., MDPI; 2020. p. 34. https://doi.org/10.3390/proceedings2020056034.

[8] Zhang L, Dong J. High-rate tunable ultrasonic force regulated nanomachining lithography with an atomic force microscope. Nanotechnology 2012;23:085303. https://doi.org/10.1088/0957-4484/23/8/085303.

[9] Deng J, Jiang L, Si B, Zhou H, Dong J, Cohen P. AFM-based nanofabrication and quality inspection of three-dimensional nanotemplates for soft lithography. J Manuf Process 2021;66:565–73. https://doi.org/10.1016/j.jmapro.2021.04.051.

[10] Deng J, Zhang L, Dong J, Cohen PH. AFM-based 3D nanofabrication using ultrasonic vibration assisted nanomachining. J Manuf Process 2016;24:195–202. https://doi.org/10.1016/j.jmapro.2016.09.003.

[11] Deng J, Dong J, Cohen PH. Development and characterization of ultrasonic vibration assisted nanomachining process for three-dimensional nanofabrication. IEEE Trans Nanotechnol 2018;17:559–66. https://doi.org/10.1109/TNANO.2018.2826841.

[12] Rahman M, Woon KS, Neo WK. Tool-based Micro/Nano machining: Development of innovative machine and machining processes. American Society of Mechanical Engineers Digital Collection; 2021. https://doi.org/10.1115/MSEC2020-8580.

[13] Geng Y, Yan Y, Brousseau E, Sun Y. AFM tip-based mechanical nanomachining of 3D micro and nano-structures via the control of the scratching trajectory. J Mater Process Technol 2017;248:236–48. https://doi.org/10.1016/j.jmatprotec.2017.05.028.

[14] Zhang L, Dong J, Cohen PH. Material-insensitive feature depth control and machining force reduction by ultrasonic vibration in AFM-based nanomachining. IEEE Trans Nanotechnol 2013;12:743–50. https://doi.org/10.1109/TNANO.2013.2273272.

[15] Xue B, Brousseau E, Bowen C. Modelling of a shear-type piezoelectric actuator for AFM-based vibration-assisted nanomachining. Int J Mech Sci 2023;243:108048. https://doi.org/10.1016/j.ijmecsci.2022.108048.

[16] Wang J, Yan Y, Geng Y, Gan Y, Fang Z. Fabrication of polydimethylsiloxane nanofluidic chips under AFM tip-based nanomilling process. Nanoscale Res Lett 2019;14:136. https://doi.org/10.1186/s11671-019-2962-6.

[17] Zhou H, Deng J. Vibration assisted AFM-based nanomachining under elevated temperatures using soft and stiff probes. Procedia Manuf 2020;48:508–13. https://doi.org/10.1016/j.promfg.2020.05.075.

[18] Geng Y, Yan Y, Zhuang Y, Hu Z. Effects of AFM tip-based direct and vibration assisted scratching methods on nanogrooves fabrication on a polymer resist. Appl Surf Sci 2015;356:348–54. https://doi.org/10.1016/j.apsusc.2015.08.068.

[19] Xue B, Geng Y, Yan Y, Ma G, Wang D, He Y. Rapid prototyping of microfluidic chip with burr-free PMMA microchannel fabricated by revolving tip-based micro-cutting. J Mater Process Technol 2020;277:116468. https://doi.org/10.1016/j.jmatprotec.2019.116468.

[20] Ma Q, Zhou H, Deng J, Wang Z. Characterizing vibration-assisted atomic force microscopy (AFM)-based nanomachining via perception of acoustic emission phenomena using a sensor-based real-time monitoring approach. Manuf Lett 2022;34:6–11. https://doi.org/10.1016/j.mfglet.2022.08.009.

[21] Steffes JJ, Ristau RA, Ramesh R, Huey BD. Thickness scaling of ferroelectricity in BiFeO3 by tomographic atomic force microscopy. Proc Natl Acad Sci 2019;116:2413–8. https://doi.org/10.1073/pnas.1806074116.

[22] Fan P, Goel S, Luo X, Upadhyaya HM. Atomic-scale friction studies on single-crystal gallium arsenide using atomic force microscope and molecular dynamics simulation. Nanomanufacturing Metrol 2022;5:39–49. https://doi.org/10.1007/s41871-021-00109-3.

[23] Lu K, Tian Y, Liu C, Zhou C, Guo Z, Wang F, et al. Design of a novel 3D ultrasonic vibration platform with tunable characteristics. Int J Mech Sci 2020;186:105895. https://doi.org/10.1016/j.ijmecsci.2020.105895.

[24] Geng Y, Brousseau EB, Zhao X, Gensheimer M, Bowen CR. AFM tip-based nanomachining with increased cutting speed at the tool-workpiece interface. Precis Eng 2018;51:536–44. https://doi.org/10.1016/j.precisioneng.2017.10.009.

[25] Tian Y, Lu K, Wang F, Guo Z, Zhou C, Liang C, et al. Design of a novel 3D tip-based nanofabrication system with high precision depth control capability. Int J Mech Sci 2020;169:105328. https://doi.org/10.1016/j.ijmecsci.2019.105328.

[26] Wang J, Yan Y, Li Z, Geng Y, Luo X, Fan P. Processing outcomes of atomic force microscope tip-based nanomilling with different trajectories on single-crystal silicon. Precis Eng 2021;72:480–90. https://doi.org/10.1016/j.precisioneng.2021.06.009.

[27] Xue B, Geng Y, Wang D, Sun Y, Yan Y. Improvement in surface quality of microchannel structures fabricated by revolving tip-based machining. Nanomanufacturing Metrol 2019;2:26–35. https://doi.org/10.1007/s41871-018-0032-9.

[28] Yan Y, Zhou E, Geng Y, He Y, Zhao X. Modelling and experimental study of nanoscratching process on PMMA thin-film using AFM tip-based nanomachining approach. Precis Eng 2018;54:138–48. https://doi.org/10.1016/j.precisioneng.2018.05.010.

[29] Geng Y, Jia J, Li Z, Liu Y, Wang J, Yan Y, et al. Modeling and experimental study of machining outcomes when conducting nanoscratching using dual-tip probe on single-crystal copper. Int J Mech Sci 2021;206:106649. https://doi.org/10.1016/j.ijmecsci.2021.106649.

[30] Wang J, Zhang Q, Yan Y, Liu Y, Geng Y. Fabrication of periodic nanostructures for SERS substrates using multi-tip probe-based nanomachining approach. Appl Surf Sci 2022;576:151790. https://doi.org/10.1016/j.apsusc.2021.151790.

[31] Geng YQ, Yan YD, Zhao XS, Hu ZJ, Liang YC, Sun T, et al. Fabrication of millimeter scale nanochannels using the AFM tip-based nanomachining method. Appl Surf Sci 2013;266:386–94. https://doi.org/10.1016/j.apsusc.2012.12.041.

[32] Wang J, Yan Y, Jia B, Geng Y. Study on the processing outcomes of the atomic force microscopy tip-based nanoscratching on GaAs. J Manuf Process 2021;70:238–47. https://doi.org/10.1016/j.jmapro.2021.08.033.

[33] Tahir U, Shim YB, Kamran MA, Kim D-I, Jeong MY. Nanofabrication techniques: challenges and future prospects. J Nanosci Nanotechnol 2021;21:4981–5013. https://doi.org/10.1166/jnn.2021.19327.

[34] Meng B, Yuan D, Zheng J, Qiu P, Xu S. Tip-based nanomanufacturing process of single crystal SiC: ductile deformation mechanism and process optimization. Appl Surf Sci 2020;500:144039. https://doi.org/10.1016/j.apsusc.2019.144039.

[35] Kumar D, Singh NK, Bajpai V. Achieving nano-patterned features by micro-EDM process using vertically aligned ZnO nanorods grown on microprobe tip: a scaling approach. Microelectron Eng 2022;260:111792. https://doi.org/10.1016/j.mee.2022.111792.

[36] Baqain S, Borodich F, Brousseau E. Theoretical study of factors affecting the effective rake angle of AFM tips for nanomachining applications. In: Yang S, Luo X, Yan Y, Jiang Z, editors. Proc. 7th Int. Conf. Nanomanufacturing NanoMan2021. Singapore: Springer; 2022. p. 131–9. https://doi.org/10.1007/978-981-19-1918-3_15.

[37] Baqain S, Borodich FM, Brousseau E. Characterisation of an AFM tip bluntness using indentation of soft materials. In: Borodich FM, Jin X, editors. Contact Probl. Soft Biol. Bioinspired Mater. Cham: Springer International Publishing; 2022. p. 221–42. https://doi.org/10.1007/978-3-030-85175-0_11.

[38] Yan Y, Li Z, Jia J, Wang J, Geng Y. Molecular dynamics simulation of the combination effect of the tip inclination and scratching direction on nanomachining of single crystal silicon. Comput Mater Sci 2021;186:110014. https://doi.org/10.1016/j.commatsci.2020.110014.

[39] Barron C, O'Toole S, Zerulla D. Fabrication of nanoscale active plasmonic elements using atomic force microscope tip-based nanomachining. Nanomanufacturing Metrol 2022;5:50–9. https://doi.org/10.1007/s41871-021-00121-7.

[40] Pellegrino P, Farella I, Cascione M, De Matteis V, Bramanti AP, Vincenti L, et al. Pile-ups formation in AFM-based nanolithography: Morpho-mechanical characterization and removal strategies. Micromachines 2022;13:1982. https://doi.org/10.3390/mi13111982.

[41] He Y, Yan Y, Geng Y. The effects of feedback control parameters on the formation of protuberances in poly(methyl methacrylate) by dynamic plowing lithography. Precis Eng 2023;81:232–9. https://doi.org/10.1016/j.precisioneng.2023.02.012.

[42] Yan Y, He Y, Xiao G, Geng Y, Ren M. Effects of diamond tip orientation on the dynamic ploughing lithography of single crystal copper. Precis Eng 2019;57:127–36. https://doi.org/10.1016/j.precisioneng.2019.03.012.

[43] Promyoo R, El-Mounayri H, Agarwal M. Experimental study of material removal at nanoscale. Procedia Manuf 2018;26:587–94. https://doi.org/10.1016/j.promfg.2018.07.069.

[44] Wang J, Yan Y, Li Z, Geng Y. Towards understanding the machining mechanism of the atomic force microscopy tip-based nanomilling process. Int J Mach Tool Manuf 2021;162:103701. https://doi.org/10.1016/j.ijmachtools.2021.103701.

[45] Wang Z, Wang X, Zhou H, Deng J. A sensor-based analytic approach for predictions of nanomachined surface profile variations via capturing temporal-spectral Acoustic Emission (AE) features for vibration-assisted Atomic Force Microscopic (AFM) based nanopatterning. Surf. Eng. Forensics 2023;12490:30–4. https://doi.org/10.1117/12.2658809. SPIE.

[46] Lu K, Tian Y, Liu C, Guo Z, Wang F, Zhang D, et al. Experimental investigation of the effects of vibration parameters on ultrasonic vibration-assisted tip-based nanofabrication. Int J Mech Sci 2021;198:106387. https://doi.org/10.1016/j.ijmecsci.2021.106387.

[47] Dyer SA, Dyer JS. Cubic-spline interpolation. 1. IEEE Instrum Meas Mag 2001;4:44–6. https://doi.org/10.1109/5289.911175.

[48] Liao Z, Xu D, Axinte D, M'Saoubi R, Thelin J, Wretland A. Novel cutting inserts with multi-channel irrigation at the chip-tool interface: modelling, design and experiments. CIRP Ann 2020;69:65–8. https://doi.org/10.1016/j.cirp.2020.04.028.

[51] Alunda BO, Lee YJ. Review: cantilever-based sensors for high speed atomic force microscopy. Sensors 2020;20:4784. https://doi.org/10.3390/s20174784.

[52] Pini V, Tiribilli B, Gambi CMC, Vassalli M. Dynamical characterization of vibrating AFM cantilevers forced by photothermal excitation. Phys Rev B 2010;81:054302. https://doi.org/10.1103/PhysRevB.81.054302.

[53] Gao F, Liu G, Wu X, Liao W-H. Optimization algorithm-based approach for modeling large deflection of cantilever beam subject to tip load. Mech Mach Theory 2022;167:104522. https://doi.org/10.1016/j.mechmachtheory.2021.104522.

[54] Wang J, Hertzmann A, Fleet DJ. Gaussian Process Dynamical Models. Adv. Neural Inf. Process. Systvol. 18. MIT Press; 2005.

[55] An online Bayesian filtering framework for Gaussian process regression: Application to global surface temperature analysis | Elsevier Enhanced Reader n.d. doi:https://doi.org/10.1016/j.eswa.2016.09.018.

[56] Bayesian variable selection for Gaussian process regression Application to chemometric calibration of spectrometers | Elsevier Enhanced Reader n.d. doi: https://doi.org/10.1016/j.neucom.2010.04.014.

[57] Diaz M, Jaramillo A, Pardo JC. Fluctuations for matrix-valued Gaussian processes. Ann Inst Henri Poincaré Probab Stat 2022;58:2216–49. https://doi.org/10.1214/21-AIHP1238.

[58] Deringer VL, Bartók AP, Bernstein N, Wilkins DM, Ceriotti M, Csányi G. Gaussian process regression for materials and molecules. Chem Rev 2021;121:10073–141. https://doi.org/10.1021/acs.chemrev.1c00022.